Journal of Materials Chemistry C

Accepted Manuscript

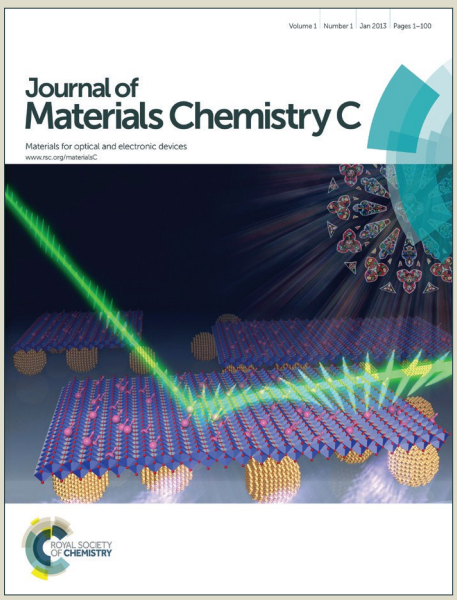

ROYAL SOCIETY OF CHEMISTRY

www.rsc.org/materialsC

The effect of Nickel doping on electron and phonon transport in n-type nanostructured thermoelectric material CoSbS

Zihang Liu[a,b], Huiyuan Geng[c], Jing Shuai[a], Zhengyun Wang[a], Jun Mao[a], Dezhi Wang[a], Qing Jie[a], Wei Cai[b], Jiehe Sui[a,b,*] and Zhifeng Ren[a*]

[a] Department of Physics and TcSUH, University of Houston, Houston, TX 77204, United States

[b] National Key Laboratory for Precision Hot Processing of Metals and School of Materials Science and Engineering, Harbin Institute of Technology, Harbin 150001, China

[c] State Key Laboratory of Advanced Welding and Joining, Harbin Institute of Technology, Harbin 150001,China

Author contributions: Z.H.L, J.H.S and Z.F.R designed the research; Z.H.L, J.S, Z.Y.W and D.Z.W performed the experiments; H.Y.G did the calculation; Z.H.L, J.M and Q.J analyzed the experiment data; Z.H.L, W.C, J.H.S and Z.F.R wrote the paper.

*To whom correspondence should be addressed. E-mail: suijiehe@hit.edu.cn, zren@uh.edu

Abstract

The effect of Ni doping on both electron and phonon transport properties of nanostructured CoSbS was investigated in this study. We found a more than 2 times increase on figure-of-merit (*ZT*). The noticeable enhancement is mainly attributed to the optimized carrier concentration, high effective mass and strong electron-phonon scattering upon Ni doping. A *ZT* of 0.5 was achieved at 873 K together with a power factor of 20 μW $cm^{-1} K^{-2}$ for the Ni doped CoSbS samples. The reduced lattice thermal conductivity via the strong electron-phonon scattering for Ni doped CoSbS samples is confirmed by the quantitative

calculation of the various phonon scattering mechanisms according to the Callaway model.

Keyword: CoSbS; Ni doping; electron-phonon scattering; thermoelectric performance.

Introduction

Thermoelectric materials and devices can directly convert heat energy into electrical energy and vice versa, and will play a significant role in the application of power generation and cooling [1-3]. The conversion efficiency of thermoelectric materials is determined by the dimensionless thermoelectric figure of merit $ZT = S^2\sigma T / (\kappa_{lat} + \kappa_{ele} + \kappa_{bip})$, where *S, σ, T,* κ_{lat}, κ_{ele}, and κ_{bip} are the Seebeck coefficient, electrical conductivity, absolute temperature, lattice thermal conductivity, electronic thermal conductivity, and bipolar thermal conductivity, respectively. For bulk thermoelectric materials, the Seebeck coefficient, electrical conductivity and electronic thermal conductivity are interrelated by carrier concentration and effective mass, which is a huge challenge to substantially improve the overall *ZT* by tailoring the aforementioned conflicting parameters [4, 5]. To enhance the *ZT* values, either increasing the power factor or lowering the thermal conductivity or both are required. The current effective methods to increase the power factor mainly include the optimization of carrier concentration [6, 7], resonant level [8, 9], band convergence [10, 11], energy barrier filtering [12], while reducing the thermal conductivity commonly benefits from solid solution [13-15], nanoscale second phase [16, 17], bulk nanostructuring [18-20], and all length-scale phonon scattering *via* hierarchical architecturing [21-23].

Despite the significant advances in bulk thermoelectric systems, the most leading thermoelectric material, such as Bi_2Te_3 [23], PbTe [6, 8, 10, 21], and SiGe [20, 25] mainly

consist of expensive elements such as Te and Ge, or toxic elements such as Pb. Due to the non-toxic, inexpensive, and ultrahigh abundance of sulfur (S), sulfur-based thermoelectric materials have drawn some attentions and their *ZT* values larger than unit have recently been achieved, especially in the p-type [26-28]. Historically, the thermoelectric performance of n-type lead-free S-based materials is not more than 0.7 at 773 K [29-34], which needs to be improved so to pair up with the p-type to make modules more efficient. In addition, most S-based thermoelectric materials including PbS exhibit a low or modest power factor less than 15 μW cm^{-1} K^{-2} [26-34]. However, large power factor should be as important as high *ZT* values for thermoelectric devices since the output power directly depends on power factor in practical power generation applications [35, 36].

CoSbS compound is a natural mineral named Costibite or Paracostibite, discovered in Canada and Australia. It crystalizes in orthorhombic space group 61 (Pbca) with a lower symmetry. There are eight [$CoSb_3S_3$] octahedral in one unit cell where one Co is octahedrally coordinated to three Sb and three S atoms as shown in Figure 1a [37]. Recently, Carlini *et al.* first reported the synthesis and microstructure of CoSbS compound [38], then, Parker *et al.* theoretically and experimentally investigated the thermoelectric performance of Ni doped CoSbS samples, with a modest power factor ~15 μW cm^{-1} K^{-2} and a relatively high thermal conductivity ~3.8 W m^{-1} K^{-1} at 773 K (A constant value Cp of 0.35 J g^{-1} K^{-1} was used to calculate the thermal conductivity) [39]. However, the specific mechanism that Ni doping boosts the thermoelectric performance of CoSbS system in the work of Parker *et al.* is still unclear. Therefore, our motivation is to systematically study the role of Ni doping on the electron and phonon transport of CoSbS system.

In our work, nanostructured CoSbS-based materials are directly prepared by high energy ball milling and hot pressing method. Our investigation shows that Ni doping on the Co lattice sites has a beneficial effect on the electron and phonon transport properties, contributing to significantly enhancing the final *ZT* value. This happen because (a) reduced electrical resistivity, (b) high density of state (DOS) effective mass and (c) increased electron-phonon scattering. First, the electrical resistivity was reduced by more than 3 orders of magnitude from 0.05 Ω m for CoSbS to 2.42×10^{-5} Ω m for $Co_{0.92}Ni_{0.08}SbS$, consistent with the fact that Ni is an electron donor to Co; Second, due to the beneficial band modification, Ni doped samples exhibit the high DOS effective mass ($m^* \sim 6.0\ m_e$) and maintain relatively high Seebeck coefficients; Third, the electron-phonon scattering is strengthened for Ni doped CoSbS, leading to the decrease of lattice thermal conductivity. Therefore, a maximum *ZT* value around 0.5 at 873 K together with a power factor about 20 μW cm^{-1} K^{-2} are obtained for Ni doped CoSbS.

Experimental

Appropriate amount of Co (99.99%), Sb (99.999%), S (99.999%), Ni (99.98%), and Se (99.98%) from Alfa Aesar were weighed according to the nominal composition and then loaded into the stainless steel jar in a glove-box under argon atmosphere. The jar was then subjected to ball-milling for 20 h. The ball-milled powder was loaded into the half-inch die and hot pressed by direct current (dc-HP) press at 1023 K for 2 min under pressure of 90 MPa.

X-ray diffraction (XRD) analysis was performed using a PANa-lytical multipurpose diffractometer with an X'celerator detector (PANalyticalX'Pert Pro). The microstructure was observed by a scanning electron microscope (SEM, JEOL6330F). The cutted bars were used for simultaneous measurement of the electrical resistivity (ρ) and Seebeck coefficient (S) on a commercial system (ULVACZEM-3). The thermal conductivity was calculated from $\kappa = DC_pd$, where D, C_p, and d are the thermal diffusivity, heat capacity, and density, respectively. The thermal diffusivity coefficient (D) was measured with the coin sample using the laser flash diffusivity method in a Netzsch LFA457 (NETZSCH, LFA457, Germany). The specific heat capacity (Cp) was measured on a differential scanning calorimetry thermal analyzer Netzsch DSC 404 C. The density (d) was determined using the Archimedes method, which was around 98% of the theoretical density of CoSbS (d = 6.8 g/cm^3). The Hall Coefficient R_H at room temperature was measured using PPMS (Physical Properties Measurement System, Quantum Design). The carrier concentration (n) was obtained by $n = 1/eR_H$ and the carrier mobility (μ) was calculated by $\sigma = ne\mu$, where σ the electrical conductivity and e is the electronic charge. Although the crystal structure of CoSbS is orthorhombic, the XRD patterns and thermoelectric properties of the parallel and perpendicular to the hot press direction demonstrate they are isotropic due to the small random grains, shown in Figures S1 and S2.

Results and discussion

Figure 1b shows the X-ray diffraction (XRD) patterns of the hot-pressed bulk samples $Co_{1-x}Ni_xSbS$ (x = 0, 0.02, 0.04, 0.06, and 0.08). All peaks exhibit good match with the

orthorhombic CoSbS (space group Pbca) without impurity phase within the detection limit of XRD spectrometer. Actually, CoSbS compound forms after ball-milling the constituent elements but the reaction did not completely finish within the ball milling time, which was demonstrated by the comparison of hot pressed CoSbS bulk disk and ball-milled CoSbS powder shown in Figure S3. Clearly, the subsequent hot-pressing completely transformed the unreacted powders into the right phase and compacted the nanoparticles into dense bulk disks. Despite the small difference between the atom radius of Co (1.25 Å) and Ni (1.24 Å), the lattice parameters of three directions gradually increased with increasing the Ni doping content, which means Ni up to 8% has indeed got into the lattice, as shown in Figure 1c. In Figure 1d, the carrier concentration monotonously increases with Ni doping by nearly 4 orders of magnitude from 3.09×10^{17} cm^{-3} for CoSbS sample to 1.13×10^{21} cm^{-3} for $Co_{0.92}Ni_{0.08}SbS$ sample. This variation is consistent with the fact that Ni has one more electron in its outer shell than that of Co. If we assume a Ni atom as a single donor based on the simple valence electron number, the theoretical carrier concentrations is obtained as the dash line depicted in Figure 1d. It can be seen the measured carrier concentrations have the same trend with but lower than the theoretical value. In addition, the mobility first sharply deceases from 4.04 cm^2 V^{-1} s^{-1} for CoSbS sample to 2.33 cm^2 V^{-1} s^{-1} for $Co_{0.98}Ni_{0.02}SbS$ sample, and then slowly decreases to 2.22 cm^2 V^{-1} s^{-1} for $Co_{0.92}Ni_{0.08}SbS$ sample. However, all the mobility data are extremely low, much lower than that of the state-of-the-art thermoelectric material such as $Pb_{0.98}Na_{0.02}Te$ (98 cm^2 V^{-1} s^{-1} at 300 K) and $Bi_2Te_{2.7}Se_{0.3}$ (173 cm^2 V^{-1} s^{-1} at 300 K) [6, 40]. The low mobility is related with the large effective mass originated from the complex band structure that will be discussed later [4, 39]. From all the

changes on XRD spectra, lattice parameter, carrier concentration, and mobility, we can safely conclude that Ni is incorporated into the CoSbS lattice.

Figure 2a shows the temperature dependent electrical resistivity of $Co_{1-x}Ni_xSbS$ samples. It is clear that the electrical resistivity for all the samples decreases with increasing temperature, displaying a typical semiconductor transport behavior. Moreover, the electrical resistivity decreased with increasing the Ni doping concentration, especially at low temperature. Typically, the electrical resistivity decreased about 3 orders of magnitude from 0.05 Ω m for undoped sample to 2.42×10^{-5} Ω m for $Co_{0.92}Ni_{0.08}SbS$ sample, due to mainly the sharp increase of carrier concentration shown in Figure 1d.

Figure 2b shows the temperature dependent Seebeck coefficient for $Co_{1-x}Ni_xSbS$ samples. For all the samples, the negative Seebeck coefficients indicate n-type semiconducting nature. The individual transport band gap of Ni doped samples are estimated by $E_g = 2e|S|_{\max} T_{\max}$, where e, S_{max}, and T_{max} is electron charge, the maximum Seebeck coefficient, and the corresponding temperature, respectively [41]. Slight reduction is observed from 0.37 eV for $Co_{0.98}Ni_{0.02}SbS$ to 0.29 eV for $Co_{0.92}Ni_{0.08}SbS$ shown in Figure 2c. This tendency is in agreement with the fact that CoSbS is a semiconductor while NiSbS is predicted to be metallic [39]. However, it is obvious that the temperature corresponding to the maximum Seebeck coefficient gradually rises when carrier concentration increases from 1×10^{20} to 1×10^{21} cm^{-3}, which is often an indication of suppression of bipolar effect. Normally, there are three strategies to suppress the bipolar effect, including increasing carrier concentration [42], enlarging band gap [43], and reducing the grain size by nanostructuring method [18]. Therefore, the suppressed bipolar effect with the increased Ni doping content

from 0.02 to 0.08 can be mainly ascribed to the sharply increased carrier concentration in this work. Narrowing the band gap should make the bipolar effect happen at lower temperature but enhanced carrier concentration makes the bipolar temperature at a higher temperature. The competing of band gap and carrier concentration determines the bipolar effect temperature. Since the effect of much enhanced carrier concentration overwhelmed that of band gap at higher doping level so the bipolar effect was in fact pushed to a higher temperature. In addtion, the Seebeck coefficient for CoSbS are rather large, namely -565 μV K^{-1} at 300 K and -200 μV K^{-1} at 873 K. Although the carrier concentration has exceeded 10^{21} cm^{-3} by heavy Ni doping, the Seebeck coefficients for Ni doped samples still maintain a relatively high value at the entire measured temperature range from -101 μV K^{-1} at 300 K to -185 μV K^{-1} at 873 K for $Co_{0.92}Ni_{0.08}SbS$. The large Seebeck coefficient for CoSbS system may be related with the high effective mass at the Fermi level (m^*). Generally, a rough estimation of the effective mass can be obtained by the following Eq. 1-3 based on the single parabolic band model [28].

$$m^* = \frac{h^2}{2k_B T}\left[\frac{n}{4\pi F_{1/2}(\eta)}\right]^{2/3} \quad (1)$$

$$S = \pm\frac{k_B}{e}\left(\frac{(r+3/2)F_{r+3/2}(\eta)}{(r+3/2)F_{r+1/2}(\eta)} - \eta\right) \quad (2)$$

$$F_n(\eta) = \int_0^\infty \frac{x^n}{1+e^{x-\eta}}dx \quad (3)$$

Where $F_n(\eta)$ is the n^{th} order Fermi integral, η the reduced Fermi energy, r the scattering factor, h the Plank constant, k_B the Boltzmann constant, x the variable of integration and e the electron charge. As acoustic phonon scattering is commonly the main scattering mechanism for most thermoelectric materials, the scattering factor r could be considered as -1/2 in

calculation [44]. The obtained effective mass (m^*) for CoSbS is 1.11 m_e, even comparable with some complex Zintl compound, including 0.8 m_e for Ca_3AlSb_3 and 1.2 m_e for $Yb_9Mn_{4.2}Sb_9$ [45, 46]. The large effective mass could be ascribed to the substantial band degeneracy near the valence and conduction band edges [39]. More significantly, the effective mass m^* for Ni doped samples $Co_{1-x}Ni_xSbS$ (x =0.02, 0.04, 0.06 and 0.08) are 6.2 m_e, 5.8 m_e, 5.9 m_e and 5.9m_e, respectively. This large increment is fully consistent with the Pisarenko plots, Seebeck coefficient as a function of carrier concentration, at room temperature shown in the Figure 2d, which are calculated using a simple parabolic band model (SPB) based on Eq. 1-3. In the Figure 2d, the black and red dashed lines represent the S - n relationship with different effective mass (m^* = 1.1 m_e and m^* = 6.0 m_e). The S – n point of undoped CoSbS locates well on the Pisarenko plots with m^* = 1.1 m_e, while the S – n points of Ni doped CoSbS lay around the Pisarenko plots with m^* = 6.0 m_e, contributing to keeping relatively high Seebeck coefficients for Ni doped samples. This difference indicates that Ni doping in the CoSbS system exhibits a beneficial influence on the band structure, which further need to be clarified by theoretical calculations.

Power factor ($PF = S^2\sigma$) calculated from the measured electrical resistivity and Seebeck coefficient is plotted in Figure 2e. A maximum power factor of 20 μW cm^{-1} K^{-2} at 873 K is obtained for $Co_{0.92}Ni_{0.08}SbS$ sample, which is 2 times that of CoSbS sample, and also about 25% higher than ~16 μW cm^{-1} K^{-2} reported by Parker *et al*. [39]. This large difference is related to the different preparation methods, ball milling vs. vacuum melting [36]. First, because Co and S elements have a big difference on melting point (1768 K and 317 K), it is more appropriate to directly use ball milling to prepare samples to avoid

volatilization of S element and the appearance of second phase. Second, the size and composition of the obtained nanoparticles after a long time ball-milling are very small and uniform and also homogenous. However, when using the vacuum-melting method, the obtained ingot sometimes possesses some inhomogeneous regions or impurity phases.

Normally, high power factor means large output power for thermoelectric devices shown in Eq. 4, which is an important criterion in practical applications in addition to *ZT*.

$$\omega = \frac{1}{4}\frac{(T_h - T_c)^2}{L} PF \quad (4)$$

where ω, T_h, T_c, and L represent the output power density, hot side temperature, cold side temperature, and leg length of thermoelectric modules, respectively. As shown in Figure 2f, the power factor of $Co_{0.94}Ni_{0.06}SbS$ are much larger than other S-based thermoelectric materials, including PbS, Cu_2S, $Cu_{12}Sb_4S_{13}$, *etc*. [26-31].

With increasing Ni doping concentration up to x = 0.08, the thermal diffusivity D shows decreased tendency at low temperature range before intrinsic excitation, as shown in the Figure 3a. Figure 3b shows the total thermal conductivity κ_{total} as a function of temperature for $Co_{1-x}Ni_xSbS$ samples. The κ_{total} of nanostructured CoSbS deceases with increasing temperature from 7.86 W m^{-1} K^{-1} at 300 K to 3.85 W m^{-1} K^{-1} at 873 K, even much higher than that of half-Heusler thermoelectric materials [47, 48]. CoSbS has the complex crystal structure and small grain size about 200 nm shown in Figure S4, meaning that the thermal conductivity should be small not high, but the observed high thermal conductivity could be ascribed to the ultrahigh average sound velocity (v_a = 4052 m/s) as a result of the light anion and stiff bonding [39]. The inversely temperature dependence of κ_{total} reveals the predominant phonon contribution to the thermal conductivity. Normally, the κ_{total} consists of

three parts, lattice thermal conductivity (κ_{lat}), electronic thermal conductivity (κ_{ele}), and bipolar thermal conductivity (κ_{bip}). As κ_{ele} can be easily calculated through the Wiedemann-Franz relationship ($\kappa_{ele} = L\sigma T$), where L is the Lorenz number, the sum of κ_{lat} and κ_{bip} could be obtained by directly subtracting κ_{ele} from κ_{total}. Herein the Lorenz number L is obtained by fitting the respective Seebeck coefficient with an estimate of the reduced chemical potential using a single parabolic band (SPB) model with acoustic phonon scattering by Eqs. 2, 3, and 5 shown in the Figure S5b [28], rather than using a constant value 2.45×10^{-8} W Ω K^{-2} for degenerate semiconductor.

$$L = \left(\frac{k_B}{e}\right)^2 \left[\frac{3F_2(\eta)}{F_0(\eta)} - \left(\frac{2F_1(\eta)}{F_0(\eta)} \right)^2 \right] \quad (5)$$

The obtained sum of κ_{lat} and κ_{bip} is plotted in Figure 3c. As it is difficult to accurately estimate the κ_{bip} simply based on the direct theoretical calculation or the linear extensional method [43, 49], κ_{lat} at low temperature range is shown in Figure 3d before the appearance of bipolar effect. As shown in Figure 3d, the κ_{lat} exhibit significant reduction upon Ni doping. For instance, the κ_{lat} at room temperature has decreased almost 20% from 6.25 W m^{-1} K^{-1} for 2% Ni doped sample to 4.98 W m^{-1} K^{-1} for 8% Ni doping. Because the difference in the atomic mass and radius between Co (58.93 g mol^{-1}, 1.25 Å) and Ni (58.69 g mol^{-1}, 1.24 Å) is quite small, the phonon scattering caused by point defects from mass and strain fluctuation could not be qualified to explain the reduction of lattice thermal conductivity. Therefore, other scattering mechanism should be responsible and deserves further investigation. In order to better understand the role of Ni doping on reduction of κ_{lat} in CoSbS system, theoretical calculation is performed according to the Callaway model [50, 51].

$$\kappa_L = \frac{k_B}{2\pi^2 v_a}\left(\frac{k_B T}{\mathrm{h}}\right)^3 \int_0^{\theta_D/T} \frac{x^4 e^x}{\tau_C^{-1}(e^x - 1)^2} dx \quad (6)$$

where x is the reduced frequency ($x = \hbar\omega/k_B$T), ω the phonon angular frequency, k_B the Boltzmann constant, v_a the average sound speed, $\hbar$ the reduced Planck constant, θ_D the Debye temperature, and τ_C the combined phonon relaxation time. θ_D and v_a values for CoSbS used in our fitting are 470 K and 4053 m/ s [39], respectively.

Four scattering mechanisms are considered in CoSbS system, including the point-defects scattering (PD), electron-phonon scattering (PE), phonon-phonon scattering (U), and grain boundary scattering (GB).

The relaxation time for point defect scattering is as follows [52]:

$$\tau_{PD}^{-1} = A\omega^4, \quad A = \frac{\delta^3 \Gamma}{4\pi v_a^3} \quad (7)$$

where v_a is the average sound speed, δ^3 the atomic volume of the compound, Γ the scattering parameter that characterizes the phonon scattering cross section of point defects. If we only consider Ni doping on Co-site in CoSbS, Γ can be written as [53, 54]

$$\Gamma = \frac{1}{3}\left(\frac{\overline{m}}{\overline{M}}\right)^2 \left[f\left(1 - \frac{m}{\overline{m}}\right)^2 + \varepsilon f\left(1 - \frac{r}{\overline{r}}\right)^2\right] \quad (8)$$

where $\overline{M}$ is the average atom weight of the compound, $\overline{m}$ and $\overline{r}$ are the average mass and radius of the substituted Co-site in the host lattice, f is the fractional concentration of Ni, m and r are the atomic weight and radius of Ni, and ε = 39, a function of the Grüneisen parameter, according to Abeles's calculation, which characterizes the anharmonicity of the

lattice.

The relaxation time for boundary scatting is:

$$\tau_{GB}^{-1} = \frac{v_a}{L} \tag{9}$$

Where L is the average grain size.

The relaxation time for phonon-phonon scatting at high temperature [52] is:

$$\tau_U^{-1} = BT\omega^2 \tag{10}$$

Where B is a constant.

The relaxation time for electron-phonon scatting [55] is:

$$\tau_{PE}^{-1} = C\omega \tag{11}$$

where C is a fitting parameter.

The combined phonon relaxation time can be expressed as:

$$\tau_C^{-1} = A\omega^4 + BT\omega^2 + C\omega + \frac{v_s}{L} \tag{12}$$

Since the value B depends only on the crystal structure of CoSbS, we obtain the precise value B by fitting Eq. 6-12 to the lattice thermal conductivity of pure CoSbS. Table 1 lists the obtained value B, as well as the calculated value A. Therefore, the only adjustable parameter C for various Ni-doping can be obtained by fitting Eq. 6-12 to the measured lattice thermal conductivity. Figure 4 shows the experimental lattice thermal conductivity with the

theoretical fitting for $Co_{1-x}Ni_xSbS$ samples, and the corresponding fitting parameters are also listed in Table 1. The theoretical model fits the experimental data well in the temperature range from room temperature to 600 K. It is clear that both the electron-phonon scattering and point-defect scattering increase drastically upon Ni doping, consistent with the obvious reduction in the carrier mobility as shown in Figure 1c.

To clarify the contribution of each scattering process to the lattice thermal conductivity, the theoretical and experimental lattice thermal conductivity of $Co_{0.92}Ni_{0.08}SbS$ is shown in Figure 5. The black dash line, red line, green dash line, and blue dash line represent the simulated κ_{lat} values considering the related scattering process – U, U + PD, U + PD + GB, and U + PD + GB + PE, respectively. As expected, the effect of point-defects scattering on κ_L is negligible. The grain boundary scattering reduces κ_L by 10%. Surprisingly, electron-phonon scattering become the most important and dominant part in CoSbS with high Ni doping concentration. The electron-phonon scattering further reduces κ_L by about 30% at room temperature. Electron-phonon scattering, which is usually assumed as a negligible part for pure semiconductors at high temperature, may become a main contribution to the reduction of lattice thermal conductivity in heavily doped semiconductors with a large effective mass, including *n*-type skutterudite $CoSb_3$ [56, 57], Half-Heusler alloys, and $Mo_3Sb_{7-x}Te_x$ [58, 59]. Deformation potential of acoustic phonons, defined as the shift in the energy of the bottom of the conduction band (or the top of valence band) per unit strain of the lattice [60], is used to characterize the strength of the electron-phonon coupling [61, 62]. High deformation potential means strong electron-phonon coupling and low mobility, and vice versa. Typically, the reported deformation potential range from 5 eV to 35 eV for

thermoelectric materials [58]. Deformation potential E_{def} can be roughly estimated by the following Eq. 13 [56, 63].

$$E_{def} = \frac{(8\pi)^{1/2}(\mathrm{h}/2\pi)^4 e\rho v_L}{3m^*(\mathrm{k_B T})^{3/2}\mu} \quad (13)$$

The obtained deformation potential E_{def} is about 38 eV, demonstrating the strong electron-phonon coupling in CoSbS system, which can also account for the unusual decrease of lattice thermal conductivity of $Co_{0.92}Ni_{0.08}SbS$.

In addition, we have estimated the minimum κ_{lat} based on the Callaway model [64].

$$\kappa_{lat} = \frac{1}{3} C_v v_a l \quad (14)$$

Where C_v, v_a, and l are the molar specific heat at constant volume, average sound velocity, and mean free path of phonons, respectively. The mean free path l was roughly estimated by the minimum interatomic distance of 2.31 Å for Co-S bond in the CoSbS system [37]. The calculated value is around 1.09 W m^{-1} K^{-1} according to Eq. 13. Since there is a large difference between our experiment result and the calculated minimum value, it is highly expected that the lattice thermal conductivity can be further lowered by choosing stronger point defects scatters or using a panoscopic approach [22, 47].

Combing the electrical and thermal properties of $Co_{1-x}Ni_xSbS$ samples, the corresponding *ZT* values are shown in Figure 6. With Ni doping to tune the carrier concentration in the range of 3.5×10^{20} - 1.3×10^{21} cm^{-3} at 900 K [39], the highest *ZT* values are about 0.5 at 873 K for three samples (x = 0.04, 0.06, and 0.08), which is 2 times that of CoSbS sample. In addition, the *ZT* value in our work is about 30% higher than that by Parker *et al.* in spite of their overestimation of *ZT* using an estimated constant Cp value (0.35) in their work. Since the lattice thermal conductivity of $Co_{1-x}Ni_xSbS$ sample is still very high,

further enhancement of *ZT* values may be expected via creating effective alloying or adding proper nanoparticles to increase the phonon scattering and thereby to further suppress the lattice thermal conductivity.

Conclusion

Undoped and Ni doped CoSbS materials were successfully prepared by high energy ball milling and hot pressing. Upon Ni doping, the carrier concentrations were increased by nearly 4 orders of magnitude from 3.09×10^{17} cm^{-3} for CoSbS to 1.13×10^{21} cm^{-3} for $Co_{0.92}Ni_{0.08}SbS$. Optimization of carrier concentration leads to noticeable decrease of electric resistivity, consequently leading to enhanced power factors. Besides, due to the beneficial band modification, Ni doped samples exhibit high effective mass ($m^* \sim 6.0\ m_e$), maintaining relatively high Seebeck coefficients; More significantly, the strong electron-phonon scattering for Ni doped samples mainly contribute to the sharp reduction of the lattice thermal conductivity in addition to nanostructuring. As a result, a maximum ZT value ~0.5 is obtained at 873 K with a power factor of 20 $\mu W\ cm^{-1}\ K^{-2}$.

Acknowledgements

The work performed at University of Houston is funded by DOE under contract number DE-FG02-13ER46917 / DE-SC0010831.

Reference

[1] D. M. Rowe, CRC Handbook of Thermoelectrics, CRC Press, Boca Raton, FL 1995.

[2] J. Yang, T. Caillat, MRS Bulletin., 2006, 31, 224-229.

[3] M. Zebarjadi, K. Esfarjani, M. S. Dresselhaus, Z. F. Ren and G. Chen, Energy Environ Sci., 2012, 5, 5147-5162.

[4] G. J. Snyder and E. S. Toberer, Nat. Mater., 2008, 7, 105-114.

[5] W. S. Liu, X. Yan, G. Chen, Z. F. Ren, Nano Energy, 2012, 1, 42-56.

[6] Y. Z. Pei, A. LaLonde, S. Iwanaga and G. J. Snyder, Energy Environ. Sci., 2011, 4, 2085-2089.

[7] J. Li, J. H. Sui, Y. L. Pei, C. Barreteau, D. Berardan, N. Dragoe, W. Cai, J. Q. He and L. D. Zhao, Energy Environ. Sci., 2012, 5, 8543-8547.

[8] J. P. Heremans, V. Jovovic, E. S. Toberer, A. Saramat, K. Kurosaki, A. Charoenphakdee, S. Yamanaka and G. J. Snyder, Science, 2008, 321, 554-557.

[9] Q. Zhang, B. Liao, Y. Lan, K. Lukas, W. Liu, K. Esfarjani, C. Opeil, D. Broido, G. Chen and Z. Ren, Proc. Natl. Acad. Sci. U. S. A., 2013, 10, 13261-13266.

[10] Y. Z. Pei, X. Y. Shi, A. LaLonde, H. Wang, L. D. Chen and G. J. Snyder, Nature, 2011, 473, 66-69.

[11] W. Liu, X. J. Tan, K. Yin, H. J. Liu, X. F. Tang, J. Shi, Q. J. Zhang and C. Uher, Phys. Rev. Lett., 2012, 108, 166601.

[12] J. P. Heremans, C. M. Thrush and D. T. Morelli, Phys. Rev. B: Condens. Matter Mater. Phys., 2004, 70, 115334.

[13] J. Yang, G. Meisner and L. Chen, Appl. Phys. Lett., 2004, 85, 1140-1142.

[14] F. Gascoin, S. Ottensmann, D. Stark, S. M. Haile and G. J. Snyder, Adv. Funct. Mater., 2005, 15, 1860-1864.

[15] G. Joshi, T. Dahal, S. Chen, H. Z. Wang, J. Shiomi, G. Chen and Z. F. Ren, Nano Energy, 2013, 2, 82-87.

[16] K. F. Hsu, S. Loo, F. Guo, W. Chen, J.S. Dyck, C. Uher, T. Hogan, E. K. Polychroniadis and M. G. Kanatzidis, Science, 2004, 303, 818-821.

[17] J. Q. He, S. N. Girard, M. G. Kanatzidis and V. P. Dravid, Adv. Funct. Mater., 2010, 20, 764-772.

[18] B. Poudel, Q. Hao, Y. Ma, Y. C. Lan, A. Minnich, B. Yu, X. A. Yan, D. Z. Wang, A. Muto, D. Vashaee, X. Y. Chen, J. M. Liu, M. S. Dresselhaus, G. Chen and Z. F. Ren, Science, 2008, 320, 634-638.

[19] W. J. Xie, X. F. Tang, Y. G. Yan, Q. J. Zhang and T. M. Tritt, Appl. Phys. Lett., 2009, 94, 102111.

[20] G. Joshi, H. Lee, Y. C. Lan, X. W. Wang, G. H. Zhu, D. Z Wang, R. W. Gould, D. C. Cuff, M. Y. Tang, M. S. Dresselhaus, G. Chen, and Z. F. Ren, Nano Lett., 2008, 8, 4670-4674.

[21] K. Biswas, J. Q. He, I. D. Blum, C. I. Wu, T. P. Hogan, D. N. Seidman, V. P. Dravid and M. G. Kanatzidis, Nature, 2012, 489, 414-418.

[22] L. D. Zhao, V. P. Dravid and M. G. Kanatzidis, Energy Environ. Sci., 2014, 7, 251-268.

[23] J. Q. He, M. G. Kanatzidis and V. P. Dravid, Mater. Today., 2013, 16, 166-176.

[24] W. S. Liu, K. C. Lukas, K. McEnaney, S. Lee, Q. Zhang, C. P. Opeil, G. Chen and Z. F. Ren, Energy Environ. Sci., 2013, 6, 552-560.

[25] X. W. Wang, H. Lee, Y. C. Lan, G. H. Zhu, G. Joshi, D. Z. Wang, J. Yang, A. J. Muto,

M. Y. Tang, J. Klatsky, S. Song, M. S. Dresselhaus, G. Chen and Z. F. Ren, Appl. Phys. Lett., 2008, 93, 193121.

[26] Y. He, T. Day, T. S. Zhang, H. L. Liu, X. Shi , L. D. Chen and G. J. Snyder, Adv. Mater., 2014, 26, 3974-3978.

[27] X. Lu, D. T. Morelli, Y. Xia, F. Zhou, V. Ozolins, H. Chi, X. Y. Zhou and C. Uher, Adv. Energy Mater., 2013, 3, 342-348.

[28] L. D. Zhao, S. H. Lo, J. Q. He, H. Li, K. Biswas, J. Androulakis, C. I Wu, T. P. Hogan, D. Y. Chung, V. P. Dravid and M. G. Kanatzidis, J. Am. Chem. Soc., 2011, 133, 20476-20487.

[29] Z. H. Liu, Y. L. Pei, H. Y. Geng, J. C. Zhou, X. F. Meng, W. Cai, W. S. Liu and J. H. Sui, Nano Energy, 2015, 13, 554-562.

[30] E. Guilmeau, Y. Bre´ard, and A. Maignan, Appl. Phys. Lett., 2011, 99, 052107.

[31] Q. Tan, L. D. Zhao, J. F. Li, C. F. Wu, T. R. Wei, Z. B. Xing and M. G. Kanatzidis, J. Mater. Chem. A., 2014, 2, 17302-17306.

[32] S. N. Guin, J. Pan, A. Bhowmik, D. Sanyal, U. V. Waghmare and K. Biswas, J. Am. Chem. Soc., 2014, 136, 12712–12720.

[33] S. N. Guin and K. Biswas, Chem. Mater., 2013, 25, 322.

[34] K. Biswas, L. D. Zhao and M. G. Kanatzidis, Adv. Energy Mater., 2012, 2, 634–638.

[35] W. S. Liu, Q. Jie, H. S. Kim and Z. F. Ren, Acta Mater., 2015, 87, 357-376.

[36] J. Shuai, H. S. Kim, Y. C. Lan, S. Chen, Y. Liu, H. Z. Zhao, J. H. Sui and Z. F. Ren, Nano Energy, 2015, 11, 640-646.

[37] L. J. Cabri, D. C. Harris and J. M. Stewart, The American Mineralogist, 1970, 55, 10.

[38] R. Carlini, C. Artini, G. Borzone, R. Masini, G. Zanicchi, and G. A. Costa, J. Therm. Anal. Calorimetry., 2011, 103, 23-27.

[39] D. Parker, A. F. May, H. Wang, M. A. McGuire, B. C. Sales and D. J. Singh, Phys. Rev. B., 2013, 87, 045205.

[40] W. S. Liu, Q. Y. Zhang, Y. C. Lan, S. Shuo, X. Yan, Q. Zhang, H. Wang, D. Z. Wang, G. Chen and Z. F. Ren, Adv. Energy Mater., 2011, 1, 577-587.

[41] H. J. Goldsmid and J. W. Sharp, J. Electron. Mater., 1999, 28, 869-872.

[42] L. P. Hu, T. J. Zhu, Y. G. Wang, H. H. Xie, Z. J. Xu and X. B. Zhao, NPG Asia Mater., 2014, 6, 88.

[43] L. D. Zhao, H. J. Wu, S. Q. Hao, C. I. Wu, X. Y. Zhou, K. Biswas, J. Q. He, T. P. Hogan, C. Uher, C. Wolverton, V. P. Dravid and M. G. Kanatzidis, Energy Environ. Sci., 2013, 6, 3346-3355.

[44] T. M. Tritt, Thermal conductivity: theory, properties, and applications, Kluwer Academic/Plenum publishers, New York, 2004.

[45] W. Zeier, A. Zevalkink, E. Schechtel, W. Tremel and G. J. Snyder, J. Mater. Chem., 2012, 22, 9826-9830.

[46] S. K. Bux, A. Zevalkink, O. Janka, D. Uhl, S. Kauzlarich, J. G. Snyder and J.-P. Fleurial, J. Mater. Chem. A., 2014, 2, 215–220

[47] G. Joshi, X. Yan, H. Z. Wang, W. S. Liu, G. Chen, Z. F. Ren, Adv. Energy Mater., 2011, 1, 643-647.

[48] X. Yan, G. Joshi, W. S. Liu, Y. C. Lan, H. Wang, S. Lee, J. M. Simonson, S. J. Poon, T. M. Tritt, G. Chen, Z. F. Ren, Nano Lett., 2011, 11, 556-560.

[49] D. M. Rowe, C. M. Bhandari, Modern thermoelectric, Reston Publishing Company, Inc.: Reston, Virginia, 1983.

[50] J. Callaway, Phys. Rev., 1959, 113, 1046.

[51] H. Y. Geng, X. F. Meng, H. Zhang, J. Zhang, Appl. Phys. Lett., 2014, 104, 202104.

[52] P. G. Klemens, Proc. Phys. Soc. Lond. A., 1955, 68, 1113-1128.

[53] B. Abeles, Phys. Rev., 1963, 131, 1906.

[54] G. A. Slack, Phys. Rev., 1962, 126, 427.

[55] S. L. Shindé, G. P. Srivastava, Length-Scale Dependent Phonon Interactions, Springer, New York, 2014

[56] H. Anno , K. Matsubara , Y. Notohara , T. Sakakibara , H. Tashiro , J. Appl. Phys., 1999, 86, 3780-3786.

[57] J. Yang , D. T. Morelli , G. P. Meisner , W. Chen , J. S. Dyck , C. Uher , Phys. Rev. B., 2002, 65, 094115.

[58] H. H. Xie, H. Wang, Y. Pei, C. Fu, X. Liu, G. J. Snyder, X. Zhao and T. Zhu, Adv. Funct. Mater., 2013, 23, 5123-5130.

[59] X. Y. Shi, Y. Z. Pei, G. J. Snyder and L. D. Chen, Energy Environ. Sci., 2011, 4, 4086-4095.

[60] A. Rose, Electron phonon interactions, World Scientific, 1989.

[61] H. Wang, Y. Z. Pei, A. D. LaLonde, and G. J. Snyder, Proc. Natl. Acad. Sci. U. S. A., 2012, 1099, 9705-9709.

[62] Y. Z. Pei, H. Wang, and G. J. Snyder, Adv. Mater., 2012, 24, 6125-6135.

[63] H. J. Goldsmid, Electronic Refrigeration, Pion, London, 1986.

[64] D. G. Cahill, S. Watson and R. Pohl, Phys. Rev. B: Condens. Matter Mater. Phys., 1992, 46, 6131-6140.

Figure Caption

Figure 1. (a) Orthorhombic structure of CoSbS with space group 61 (Pbca). The red, blue, and green spheres represent Co, Sb, and S atoms, respectively. (b) XRD patterns of bulk $Co_{1-x}Ni_xSbS$ (x = 0, 0.02, 0.04, 0.06, and 0.08), (c) lattice parameter as a function of Ni doping content, (d) room temperature carrier concentration and mobility as a function of Ni doping content.

Figure 2. Temperature dependent electrical transport properties for $Co_{1-x}Ni_xSbS$ samples. (a) Electrical resistivity; (b) Seebeck coefficient; (c) Transport band gap estimated by the Goldsmid-Sharp formula; (d) Room temperature Pisarenko plots ; (e) Power factor; (f) Power factor of $Co_{0.94}Ni_{0.06}SbS$ in comparison with other S-based thermoelectric materials. The inserts separately show the electrical transport properties of undoped CoSbS.

Figure 3. Temperature dependent thermal transport properties for $Co_{1-x}Ni_xSbS$ samples. (a) Thermal diffusivity D; (b) total thermal conductivity κ_{total}; (c) the sum of lattice thermal conductivity κ_{lat} and bipolar thermal conductivity κ_{bip}; (d) lattice thermal conductivity κ_{lat}.

Figure 4. Fitting results of lattice thermal conductivity κ_L for $Co_{1-x}Ni_xSbS$ samples based on the Callaway model.

Figure 5. Contribution of various scattering processes to the lattice thermal conductivity κ_L of $Co_{0.92}Ni_{0.08}SbS$ sample.

Figure 6. Temperature dependent *ZT* values for Ni doped CoSbS samples.

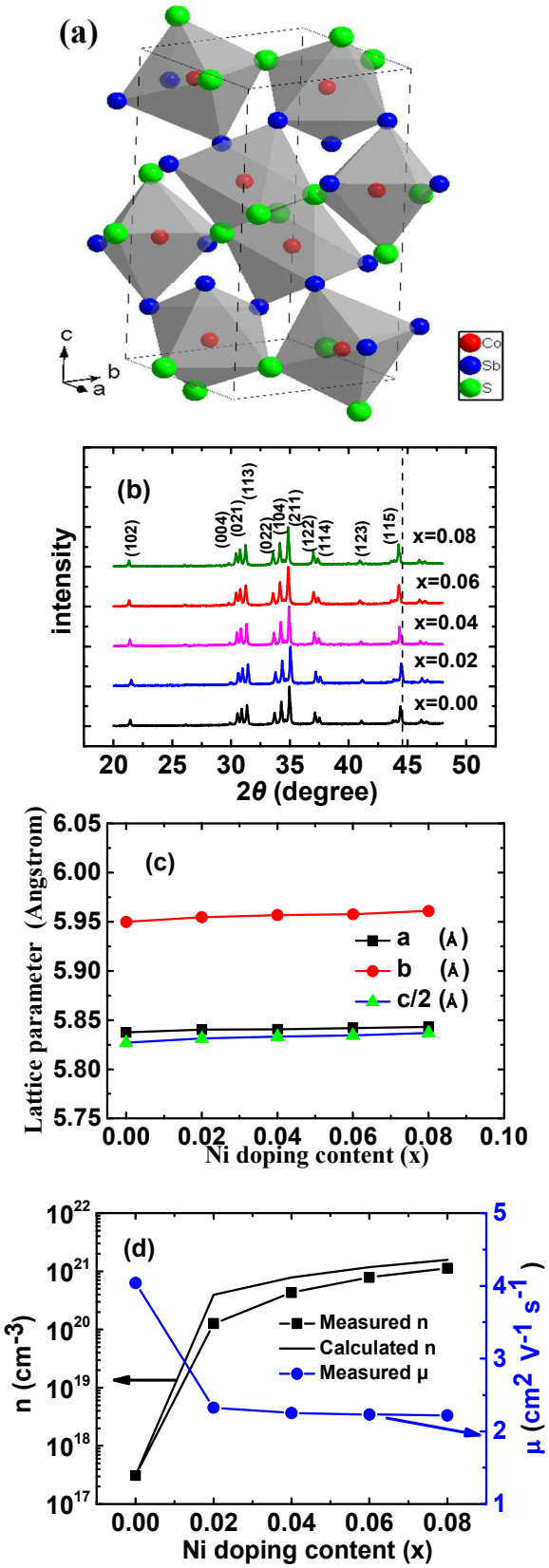

Figure 1

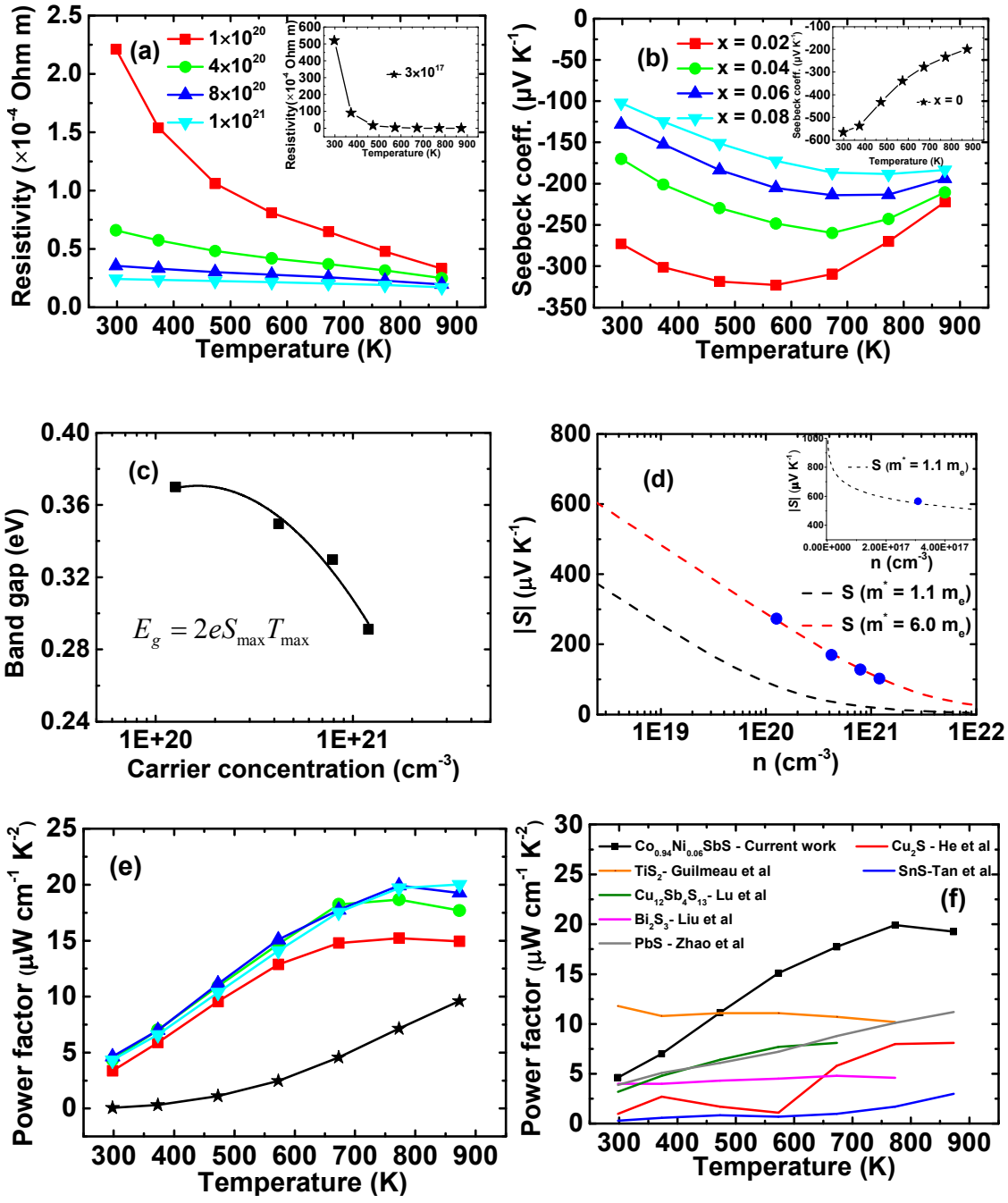

Figure 2

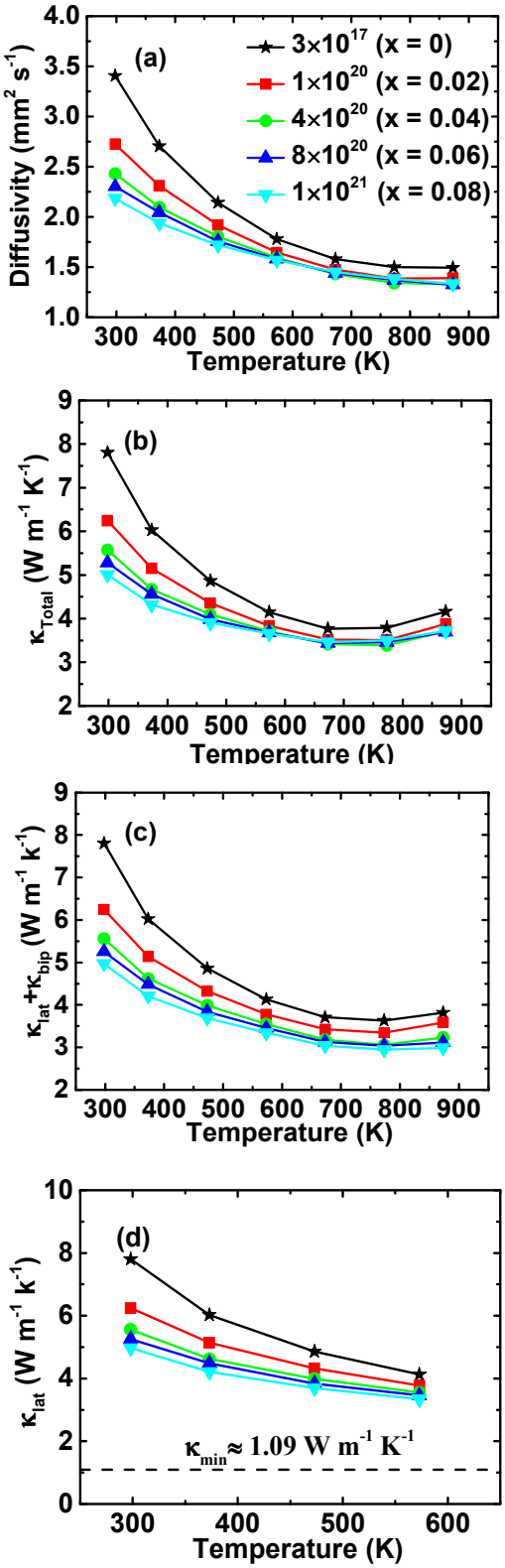

Figure 3

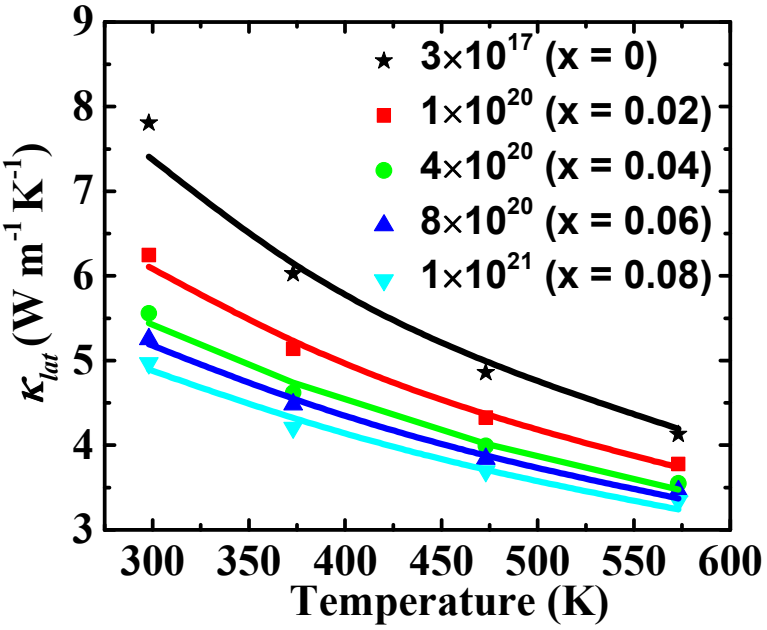

Figure 4

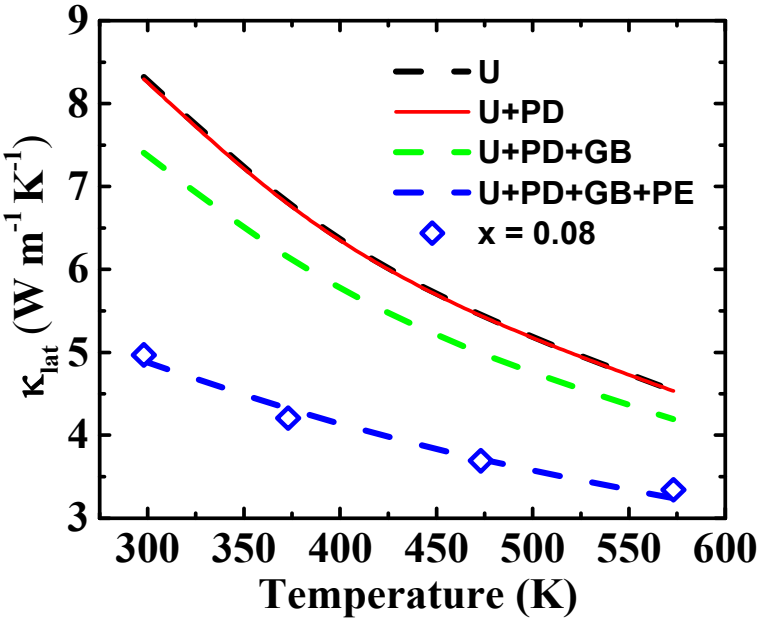

Figure 5

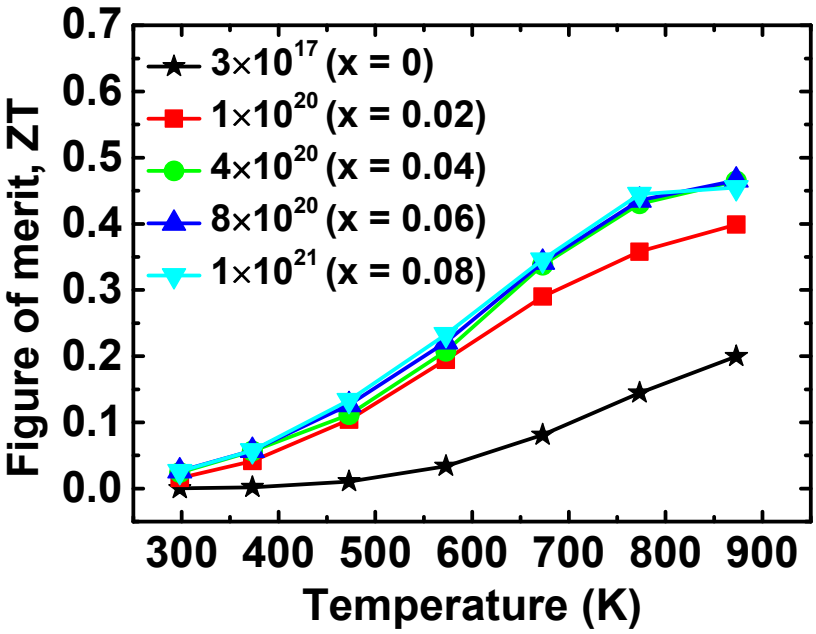

Figure 6

Table

Table 1. Fitting parameters of lattice thermal conductivity κ_L as defined by Equation 6-12.

Composition	A (10^{-46} s^3)	B (10^{-18} sK^{-1})	C (10^{-4})
x = 0	0	4.01	1.1×10^{-3}
x = 0.02	8.77	4.01	66.41
x = 0.04	17.35	4.01	116.71
x = 0.06	25.52	4.01	139.31
x = 0.08	33.29	4.01	170.16

Graphical Abstract